



ELSEVIER

Physica D 98 (1996) 287–300

PHYSICA D

Some unexpected consequences of the interaction between convective adjustment and horizontal diffusion

Paola Cessi *, W.R. Young

Scripps Institution of Oceanography, La Jolla CA 92093-0230, USA

Abstract

We consider the dynamics of a set of diffusively coupled “grid points”. The dependent variable defined at each grid point is the salinity which is forced by a spatially uniform distribution of evaporation minus precipitation. The nonlinearity in the system is a convective adjustment rule that sets the salinity back to zero if it ever exceeds one. The aim of this study is to understand the spatial and temporal variability that results from the interaction between convective adjustment rules and horizontal diffusivity.

Analytic results show that the model has a large number of different solutions which are periodic in space and time. Some of these solutions have a surprising structure in which convective adjustment is entirely suppressed at some grid points, and occurs with a higher frequency at neighboring points. Numerical solutions indicate that these solutions have finite basins of attraction in the space of initial conditions. Thus small changes in the initial conditions can produce solutions with grossly different average properties.

Numerical errors due to the finite size of the time step, or roundoff, can also have a decisive role in selecting the ultimate state which emerges from a particular condition. For instance, numerical errors can stabilize an unstable solution.

Keywords: Convective adjustment; Coupled map lattices

1. Introduction

In ocean general circulation models, static instabilities (heavy fluid over light) are removed by a “convective adjustment” (CA) algorithm. The essential idea is that when a density inversion is detected one rapidly mixes temperature and salinity to produce a neutrally stable state [1]. In this article we investigate some consequences of the interaction between two widely accepted model ingredients, namely CA rules and horizontal diffusion.

There are different implementations of CA algorithms (e.g., [2,3]) but one common aspect is that the decision to adjust ignores *horizontal* differences in density. Thus, if CA occurs at one grid point, but not at a neighboring grid point, then a grid-scale density jump is created very rapidly – perhaps in a single time step depending on the CA algorithm.

We illustrate the effects of these density jumps in Fig. 1. In Fig. 1(a) the density at all of the grid points is increasing so that eventually the threshold for adjustment will be reached. The first grid point to reach this threshold is the density maximum at $n = 0$. In Fig. 1(b) we show the situation a short time later in which there is now a large jump in density between

* Corresponding author. Tel.: 619 534 0622; fax: 619 534 9820; e-mail: cessi@dalek.ucsd.edu.

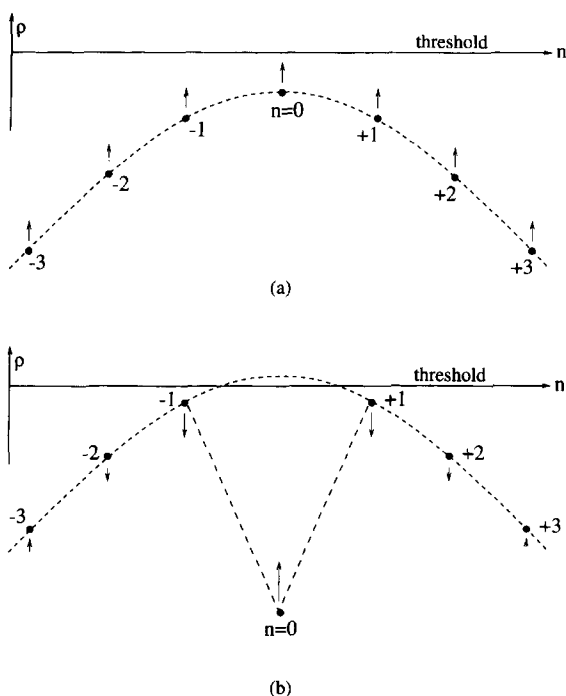


Fig. 1. A schematic showing the result of convective adjustment. The vertical axis is density and the horizontal axis is the grid point position. (a) All of the grid points are advancing upwards towards the threshold for adjustment: this increase in density is driven by a preponderance of evaporation over precipitation so that the salinity of the layer is increasing. The point $n = 0$ is a local density maximum and it will adjust first. Immediately after adjustment the density at $n = 0$ will be equal to the density of the very deep, cold and fresh reservoir layer, i.e., the column is neutrally stable. But then thermal coupling to the atmosphere very rapidly increases the temperature at $n = 0$, but leaves the low salinity behind. The result is that the density at $n = 0$ is now stable because of the freshwater imported from the deep reservoir: this is the configuration shown in panel (b). Because of diffusive coupling with the neighboring grid points the point at $n = 0$ tends to drag its neighbors away from the threshold.

$n = 0$ and its immediate neighbors $n = \pm 1$. After adjustment, horizontal diffusion will smooth the discontinuity in density. This horizontal flux of density will tug the nonadjusted grid points, $n = \pm 1$, away from the threshold. Thus in Fig. 1(b) the grid points $n = \pm 1$ can vacillate: while they are close to the threshold they are also diffusively fluxing density to $n = 0$ and this tendency is stabilizing. The same stabilizing tendency will also be felt in an attenuated form at increasingly removed grid points $n = \pm 2$ etc. We indi-

cate this in Fig. 1(b) by showing that the grid points at $n = \pm 1$ and ± 2 are moving away from the threshold, while those at $n = \pm 3$ are still moving towards the threshold.

The upshot of all this is that in Fig. 1(b) it is unclear if the grid points $n = \pm 1$ will soon adjust or not. We show in this paper that this uncertainty produces intrinsic time dependence and spatial nonuniformities in the thermohaline fields. We find that the variability driven by this mechanism produces a curious coupling between the largest and the smallest spatial scales in the model. The CA rule, because it is applied at a single grid point, transfers density variance directly to the model grid scale without any intermediate cascade through wave number space.

Fig. 1 also illustrates the possibility of making an inaccurate application of the CA rule. Suppose that an accurate solution of the system leads to the situation in Fig. 1(b), in which the grid points $n = \pm 1$ are moving away from the threshold. A numerically inaccurate solution might lead to the three grid points $n = 0$ and $n = \pm 1$ all passing over the threshold in a single time step. In this case the CA algorithm will set all three grid points equal to the same value and this state differs appreciably from the accurate solution in Fig. 1(b).

We believe that the thermohaline variability described above is an unrealistic aspect of the CA procedure in ocean general circulation models. Convection in the ocean certainly produces interesting large scale thermohaline structure. But the thermohaline variability documented in this paper is best described as a pathology of the CA algorithm, rather than the result of a plausibly parameterized physical process. Unfortunately we have not been able to formulate an entirely satisfactory alternative to the standard procedure. Our goal here is less ambitious: we will document the consequences of the mechanism in Fig. 1 so that it can be recognized when it operates in ocean circulation models.

Our discussion of CA has been from the perspective of an ocean modeler or numerical analyst. But the system we will formulate in Section 2 turns out to have some unexpected affinities with coupled lattice models (e.g., [4,5]). We will return to this interesting analogy after formulating the model.

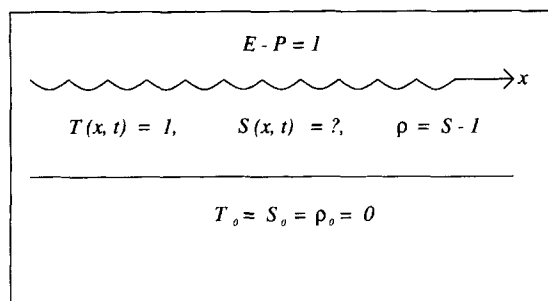


Fig. 2. A scenario leading to the model in (2.1a), (2.1b). The upper layer has a fixed temperature $T = 1$ and an evolving salinity $S(x, t)$ so that the density is $\rho = S - 1$. The evaporation minus precipitation forcing on the upper layer is spatially uniform and equal to one. The lower layer is very deep with infinite capacity and $S = T = \rho = 0$. Fast mixing with the lower layer occurs when $S(x, t)$ exceeds one.

2. Formulation of the model

We use the model introduced by Cessi [6] which is a collection of spatially coupled “convective adjustment oscillators”:

$$S_t = 1 + \alpha S_{xx} + \text{CA} \quad \text{if } S \leq 1, \quad (2.1a)$$

$$S \rightarrow 0 \quad \text{if } S > 1, \quad (2.1b)$$

where $0 < x < 1$. For simplicity we ignore end-effects by considering periodic systems with $S(x, t) = S(x + 1, t)$.

An oceanographic scenario leading to (2.1) is illustrated in Fig. 2: $S(x, t)$ is the salinity in an upper layer of fluid with fixed temperature $T = 1$. The very deep, lower layer has $T = S = 0$. We use a linear equation of state in which the density $\rho = S - T$ so that the density of the lower layer is zero and the density of the upper layer is $S - 1$. The first term on the right-hand side of (2.1a) represents the imbalances between evaporation and precipitation ($E - P$ in Fig. 2) that tend to destabilize the layer by steadily increasing its salinity. The second term on the right-hand side of (2.1a) is diffusive coupling. The final term, CA, in (2.1a) is to remind us that the model has appended to it the rule in (2.1b): the model is strongly nonlinear despite the superficially linear structure of (2.1a).

The temperature in the upper layer is clamped to the value 1 while the salinity evolves so that we are considering the scenario in which thermal relaxation

is much more rapid than saline relaxation (e.g., [1,7]). This is the fundamental asymmetry between heat and salt in this system. Now suppose that there is some point where the salinity, $S(x, t)$, of the upper layer exceeds the temperature, $T = 1$. Then at that position the density of the upper layer is greater than the density of the lower layer and the ensuing static instability produces instantaneous mixing. This rapid mixing is encoded by the CA rule in (2.1b) which sets the salinity of the upper layer equal to that of the very deep lower layer.

Contrary to the suggestion in Fig. 2, oceanographic convection is not often driven by evaporation. A more common scenario is polar convection in which the surface is cooled and freshened so that heat, rather than salinity, is the destabilizing component. However, analogous dynamics can be obtained in the thermally driven case if one considers the effects of a nonlinear equation of state (e.g., [8,9]). We prefer to use the salinity driven model because it is conceptually simple and avoids nonessential complications such as a realistic equation of state.

The problem in (2.1a), (2.1b), and particularly the adjustment rule, has to be understood in the context of a discretized model. In fact, as it stands, the model in (2.1) would offend a traditional numerical analyst. For instance, S_{xx} is not defined after one applies the rule in (2.1b). Or perhaps it is better to say that it is not clear how this rule can be implemented in a continuous model. This criticism applies with equal force to all ocean general circulation models that use CA, beginning with that of Bryan in [10]. However, in our opinion, this difficulty with the continuous limit is not, by itself, a trenchant objection to the CA algorithm. The point is that one can interpret the model as a set of coupled equations obtained by spatially discretizing (2.1a). Thus we divide the interval $0 < x < 1$ into N subregions of length $1/N$ so that $x = n/N$ where $1 < n < N$. The state of the system at time t is defined by the N -component vector $S_n(t)$ and this vector evolves according to

$$\dot{S}_n = 1 + \alpha N^2 [S_{n+1} - 2S_n + S_{n-1}] \quad \text{if } S_n \leq 1, \quad (2.2a)$$

$$S_n \rightarrow 0 \quad \text{if } S_n > 1. \quad (2.2b)$$

For numerical implementation one has to also discretize (2.2a) in time. But for expositional purposes we distinguish the semi-discrete form in (2.2) from the fully discrete form in (2.3) and (2.4) below.

We now discretize (2.2) in time using the simplest scheme: forward Euler. Given the present state $S_n(t)$ we define the tentative future state by

$$\hat{S}_n(t + \tau) \equiv S_n(t) + \tau + (\mu\tau) [S_{n+1}(t) - 2S_n(t) + S_{n-1}(t)], \quad (2.3)$$

where τ is the time step and $\mu \equiv \alpha N^2$. We then apply CA and obtain the true future state by using the rule:

$$S_n(t + \tau) = \hat{S}_n(t + \tau) \quad \text{if } \hat{S}_n(t + \tau) \leq 1, \quad (2.4a)$$

$$S_n(t + \tau) = 0 \quad \text{if } \hat{S}_n(t + \tau) > 1. \quad (2.4b)$$

Eqs. (2.3) and (2.4) define the algorithm used in the numerical calculations in this paper.

The explicit time-stepping procedure in (2.3) has a well-known numerical instability if τ is too large. Specifically, in order to suppress the “computational mode”, the time step must satisfy the inequality

$$\mu\tau < \frac{1}{4}. \quad (2.5)$$

All the simulations in this paper will satisfy the condition in (2.5).

At this point we can draw an analogy between the fully discrete system and the coupled map lattices studied by Keeler and Farmer [4] and Crutchfield and Kaneko [5]. A coupled map lattice is a dynamical system with discrete time, discrete space and continuous state. In the examples referenced above the coupling is diffusive between nearest neighbors. The system in (2.3) and (2.4) is then a special case of a coupled map lattice. In the world of lattice maps the term “local dynamics” refers to what happens at a single point if one removes all coupling to the neighbors, i.e., set $\alpha = 0$ in (2.2). Our model in (2.3) and (2.4) is simple because the local dynamics at each site is periodic in time. Other examples of coupled map lattices assume that the local dynamics is more interesting. The quadratic map is a popular choice so that in this case the local dynamics can be chaotic rather than simply periodic.

Coupled map lattices are intended to model and characterize space–time intermittency such as the presence of localized patches of turbulence in an otherwise laminar fluid flow. Localized oceanic convection is a naturally occurring example of this phenomenon. In this sense Bryan’s introduction of convective adjustment in 1969 seems to be a farsighted anticipation of coupled map lattices!

3. Some simulations

3.1. The synchronized solution and the grid mode

The semi-discrete model in (2.2) has a simple solution in which all of the S_n ’s are equal,

$$S_n = t - \text{int}(t), \quad (3.1)$$

where $\text{int}(t)$ is the integer part of t , e.g., $\text{int}(\pi) = 3$. In this spatially uniform solution all of the grid points are in phase and synchronized adjustment occurs at $t = 1, 2, 3$, etc. This spatially uniform solution is analogous to the thermohaline relaxation oscillations whose dynamics were first isolated by Welander [11] with the “flip-flop” model (e.g., [12]).

It can be shown analytically that the synchronized solution in (3.1) is unstable to a grid-scale instability, such that all the even grid points adjust out of phase of the odd ones [6]. In order to motivate some analytic solutions in Section 4 we recall some aspects of Cessi’s analysis. One can find a solution which is periodic in space with $S_{2n}(t) = a(t)$ and $S_{2n+1}(t) = b(t)$, so that the wavelength is two intervals. With this simplification the system is described by a point in the (a, b) space. We now construct a time periodic solution following the lead in Fig. 3. We suppose that at $t = 0$ the even grid points have just adjusted so that $a(0) = 0$ and $b(0) = B$. For a periodic solution it turns out that the next adjustment is at $t = \frac{1}{2}$ and at this time $a(\frac{1}{2}) = B$ and $b(\frac{1}{2}) = 1 \rightarrow 0$. In the next interval, $\frac{1}{2} < t < 1$, the roles of a and b are reversed.

To determine the constant B notice that the solution of (2.2a) in the interval $0 < t < \frac{1}{2}$ is

$$\begin{pmatrix} a \\ b \end{pmatrix} = t \begin{pmatrix} 1 \\ 1 \end{pmatrix} + \frac{B}{2} \begin{pmatrix} 1 \\ 1 \end{pmatrix} + \frac{B}{2} \begin{pmatrix} -1 \\ 1 \end{pmatrix} e^{-4\mu t}, \quad (3.2)$$

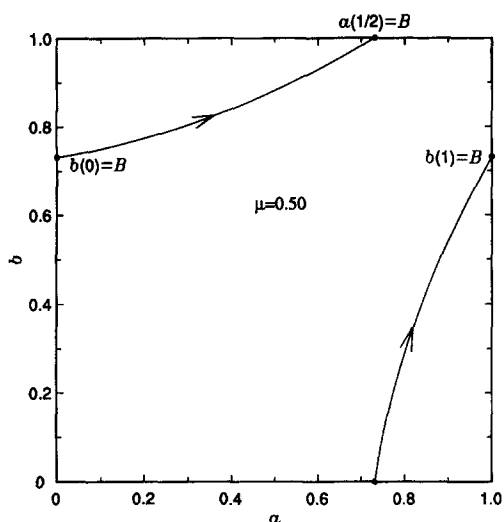


Fig. 3. The phase plane of the grid mode, b as a function of a , both given by (3.2) for one cycle of the oscillation. At $t = 0$, a has just adjusted and $b(0) = B$, given by (3.3). At $t = \frac{1}{2}$ the system reaches the point $(B, 1)$ and at this instant b adjusts instantly, bringing the system to $(B, 0)$. Next, at $t = 1$, a adjusts and the system reaches $(1, b(1) = B)$.

where $\mu \equiv \alpha N^2$. Putting $t = \frac{1}{2}$ into (3.2) gives

$$B = \frac{1}{1 + \exp(-2\mu)}. \quad (3.3)$$

Cessi [6] analyzed the stability of the periodic solution above to synchronizing perturbations by calculating the return map for arbitrary orbits in the (a, b) plane. Her conclusion was that the periodic solution in Fig. 3 is stable and the synchronized solution in (3.1) is unstable for all values of $\mu = \alpha N^2$.

This “grid mode” is periodic in space with a wavelength $n = 2$ and periodic in time with a period of 1. The grid mode is a frequently observed modulation in chains of coupled map lattices (e.g., [5]). In the coupled map lattice literature the grid mode is referred to as “zig-zag” instability. We believe that the solution above may well be the simplest example that isolates the basic physics of this widely observed instability.

3.2. Roundoff suppression of the grid mode

We mentioned in the discussion surrounding (2.5) that numerical stability requires that $\mu\tau < \frac{1}{4}$. But numerical stability is not the same as numerical accuracy

and this distinction is particularly important in determining the stability of the grid mode in the fully discrete system (2.3) and (2.4). We see from Fig. 3 that an accurate application of the CA rule at $t = \frac{1}{2}$ requires distinguishing the difference between $B(\mu)$ and 1, else one might accidentally adjust both a and b back to zero and latch on to the synchronized solution in (3.1). When μ is large $1 - B \approx \exp(-2\mu)$, so that the accurate solution of (2.2) requires that the time step satisfy the inequality

$$\tau < e^{-2\mu}. \quad (3.4)$$

When $\mu = \alpha N^2 \gg 1$ the accuracy condition in (3.4) is much more stringent than the stability condition in (2.5). In fact, as the spatial resolution is increased the condition in (3.4) soon becomes burdensome.

What happens if the time-step violates (3.4), but still satisfies the condition for numerical stability? That is, suppose the time step satisfies the double inequality:

$$e^{-2\mu} < \tau < 1/4\mu. \quad (3.5)$$

In this case, as we have explained above, very small numerical errors have large effects because the CA rule in (2.2b) is occasionally applied inaccurately. We have argued that the result of these errors is a tendency to suppress the grid mode and establish the synchronized solution.

The grid mode is an anathema to all sensible numerical schemes. It is alarming to discover that the CA algorithm can excite this mode and it is curious that roundoff errors can correct this problem by suppressing the grid mode. Roundoff error operates in ocean general circulation models, and it is interesting to see what happens in our simple model if the time step satisfies the inequality in (3.5). In this case our numerical scheme is accurately solving the differential equations in (2.2a) but the scheme is inaccurately applying the rule in (2.2b). We expect that the resulting roundoff suppression is equivalent to having some very small random fluctuations, on the order of the machine precision, in either the forcing rate, or in the salinity of the deep lower layer in Fig. 2. It is beyond the scope of this communication to pursue this suggestion systematically by adding controlled amounts of extrinsic

noise to the model (2.2). Instead we focus solely on the effects of roundoff errors.

3.3. Some solutions illustrating the effect of initial conditions

As an example of what can happen when the time step satisfies the double inequality in (3.5), suppose that $\alpha = 0.03$ and $N = 100$ so that $\exp(-2\alpha N^2)$ is below machine precision. We use a time step $\tau = (128N^2)^{-1}$. With this parameter setting we do not observe the grid mode. Instead the system (2.3) and (2.4) exhibits a bewildering variety of qualitatively different asymptotic attractors and we find that the initial condition, $S_n(0)$, plays a decisive role in selecting the ultimate state. This multiplicity of attractors is reminiscent of coupled map lattices [5].

Consider initial conditions of the form

$$S_n(0) = 1 - p + p \sin^2 \left[q\pi \frac{(n + \varphi)}{N} \right]. \quad (3.6)$$

In Fig. 4 we summarize the results of four calculations with different initial conditions from the family in (3.6) by showing the points in the (n, t) plane at which the CA rule in (2.4) has been applied. In panel (a) of Fig. 4 we see that the synchronized solution in (3.1) emerges after some transient activity.

Panels (b) and (c) of Fig. 4 show examples in which the adjustment events occur apparently at random except for a few grid points at which CA occurs with greater frequency than in the background. In panel (b) there are four such “adjustment centers” at $n = 20$, 45, 70 and $n = 95$. The points $n = 20$ and $n = 70$ are maxima in the initial condition while $n = 45$ and $n = 95$ are minima in the initial condition. In panel (c) of Fig. 4 there are two adjustment centers which are located at the maximum and minimum of the initial condition. Adjustment is suppressed, but not entirely eliminated, at the grid points that neighbor the adjustment centers.

Panel (d) of Fig. 4 displays another possibility: there is a solution that is periodic in both space and time. We refer to such doubly periodic solutions as “structured”. In the structured solution in Fig. 4(d) CA occurs only at 44 of the 100 grid points and the adjustment at each

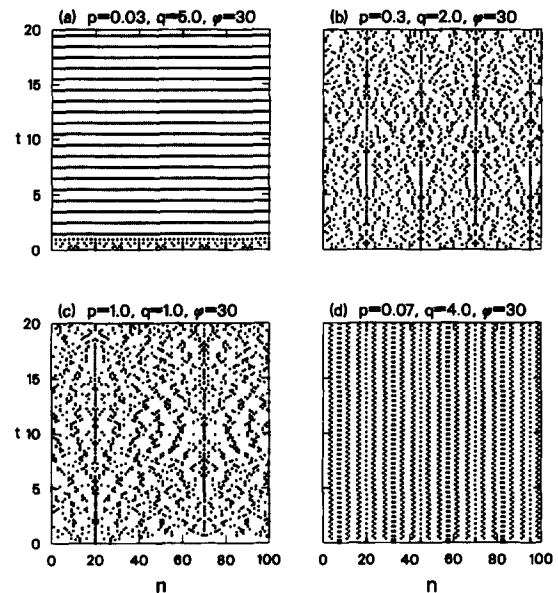


Fig. 4. The space–time coordinates of the convective adjustment events, for four numerical integrations of (2.3) and (2.4) with $\alpha = 0.03$, $N = 100$, $\tau = 1/(128N^2)$. The initial condition for all the calculations is given by (3.6) and each has a different value of p and q . (a) For $p = 0.03$ and $q = 5$ after an initial excitation of the grid mode, the system synchronizes and the spatially homogeneous solution (3.1) is obtained. (b) For $p = 0.3$ and $q = 2$, there are four preferred points of adjustment located at the maxima and minima of the initial conditions, while a lower level of random CA activity takes place at all the other grid points. (c) For $p = 1.0$ and $q = 1$, two preferred points of adjustment emerge, located at the extrema of the initial condition. The other grid points experience the same level of weak, random CA as in the case shown in (b). (d) For $p = 0.07$ and $q = 4$, CA occurs periodically in time at 44 selected grid points, while the other grid points never experience CA. The salinity is periodic in time and space.

of those 44 sites is periodic in time with the same period at each site.

A close examination of panels (b) and (c) of Fig. 4 shows that the adjustment events are symmetrically distributed around the adjustment centers. The background is not as random as it might seem at a first glance. In panel (a) of Fig. 5 we show snapshots of the four simulations in Fig. 4 at the final time $t = 20$. The spatial symmetry of S_n is also apparent in this figure. Panel (b) of Fig. 5 shows snapshots of the simulation from Fig. 4(b) at five different times. This figure also shows that the salinity seems to hover just below the threshold for adjustment, $S = 1$. This impression

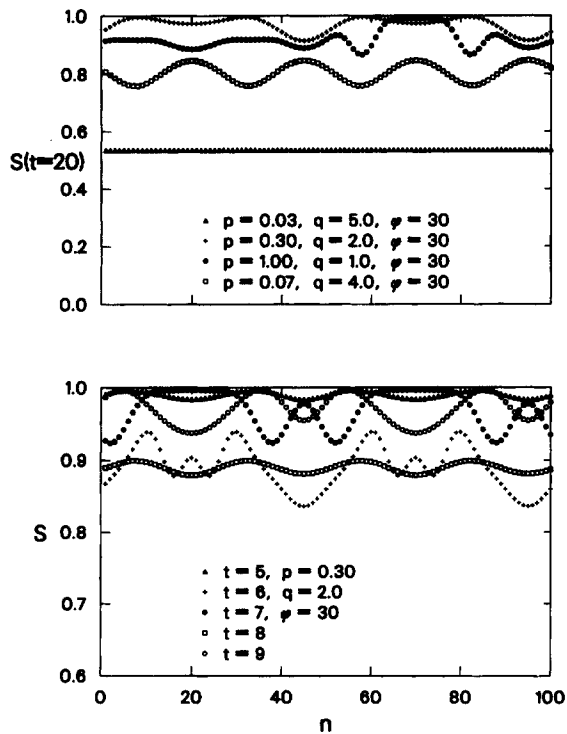


Fig. 5. Upper panel: The salinity at the final time, $S_n(t = 20)$, for the four simulations of Fig. 4. Notice the symmetry around the preferred centers of adjustment of the instantaneous salinity for the calculations of Figs. 4(b) (shown here with crosses) and (c) (shown here with filled circles). Lower panel: The salinity at five different times for the simulation of Fig. 4(b): The salinity is fluctuating near and below the CA threshold and is symmetric around the four centers of adjustment (located at $n = 20, 45, 70$ and 95).

is confirmed when we examine the spatially averaged salinity.

The spatially averaged salinity is

$$\bar{S}(t) \equiv \frac{1}{N} \sum_{n=1}^{n=N} S_n(t). \quad (3.7)$$

Figure 6 shows time series of $\bar{S}(t)$ for the four initial conditions used in Fig. 4. The upper panel of Fig. 6 shows the two periodic solutions in Figs. 4(a) and (d). The solution in Fig. 4(d) oscillates within the range $0.75 < \bar{S} < 1$ while the synchronized solution has a sawtooth oscillation over the complete range $0 < \bar{S} < 1$, e.g., (3.1). The lower panel of Fig. 6 shows the “random” solutions from Figs. 4(b) and (c). It is clear that the solution in Fig. 4(c) has smaller fluctuations

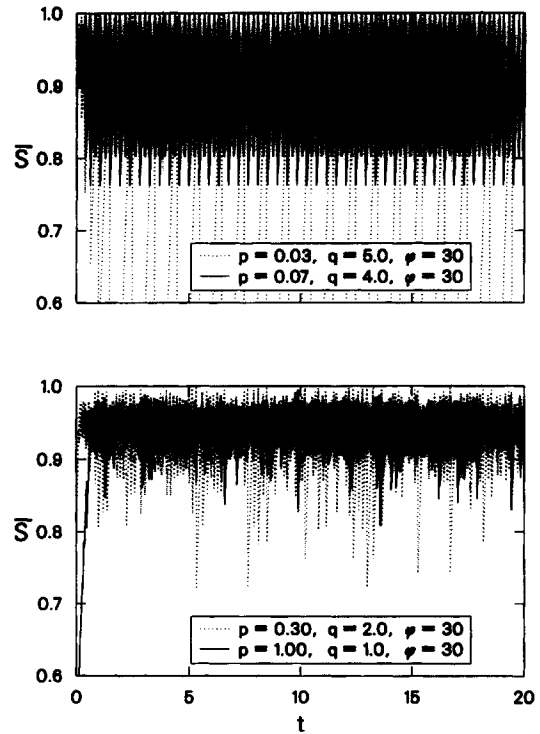


Fig. 6. The mean salinity $\bar{S}(t)$ as a function of time for the four simulations shown in Fig. 4. Upper panel: the mean salinity for the time-periodic calculations described in Figs. 4(a) and (d). The synchronized solution (dotted line) oscillates between 0 and 1, while the partially synchronized solution (solid line) oscillates between 0.75 and 1 at twice the frequency. Lower panel: the mean salinity for the calculations described in Figs. 4(b) and (c) fluctuate around and below the CA threshold and the solution with four centers of adjustment (dotted line) has larger fluctuations than that with two CA centers (solid line).

than that of Fig. 4(b). But both solutions hover close to, but below, the threshold at $S = 1$. In this sense the solutions are close to a state of marginal stability.

3.4. Random initial conditions

The four solutions shown in Figs. 4–6 all derive from the family of initial conditions in (3.6). We thought that the adjustment centers and the spatial symmetries might be inherited from these organized initial conditions. We now show that random initial conditions also produce patterns with adjustment centers.

As in the previous three figures we use $\alpha = 0.03$, $N = 100$ and $\tau = 1/(128N^2)$. The initial value of

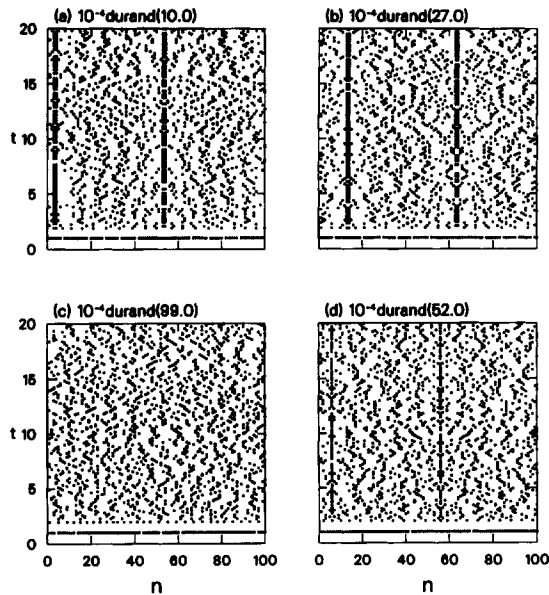


Fig. 7. The space–time locations of the adjustment events for $\alpha = 0.03$, $N = 100$, $\tau = 1/(128N^2)$. The initial condition is a random number uniformly distributed between 0 and 0.0001. Four different realizations are shown each with a different seed in the random number generator (the ESSL subroutine DURAND). Some random initial conditions lead to the emergence of adjustment centers.

S at each grid point is a random number uniformly distributed in the interval $0 < S_n(0) < 10^{-4}$. Fig. 7 shows four different realizations obtained by using four different seeds in the ESSL subroutine DURAND. In Figs. 7(a), (b) and (d) we see that adjustment centers emerge from the random initial condition. Also the pattern of adjustment events is symmetric about these centers once they appear. Note also that the adjustment centers in Figs. 7(a) and (b) consist of two adjacent grid points locked together, while in Fig. 7(d) the adjustment centers consist of a single grid point. Fig. 7(c) shows an apparently random set of events with no fixed centers.

3.5. Sensitivity to time step and changes in diffusivity

All the above results were obtained using a time step of $\tau = 1/(128N^2)$. We have repeated many of them both doubling and halving the time step and we have found that the results are insensitive to these changes.

For instance, if we repeat the calculation which produced the solid curve in the lower panel of Fig. 6(b) with half the time step and double the time step we find that the three graphs of $\bar{S}(t)$ coincide to within the line width of the plot up till at least $t = 14$. After this time the three curves spread apart but the statistical behavior of the three cases seems to be identical in so far as all three time series fluctuate about the same average level with the same RMS ΔS . A closer examination of the growth of the difference between the three cases shows that the difference is growing exponentially with time.

We also were curious about the effect of increasing the diffusivity α . If we increase the diffusivity by a factor of 10 to $\alpha = 0.3$ and repeat the calculations in Fig. 7 then we find that all four initial conditions eventually become synchronized as in Fig. 4(a). However, if we take the same four random initial conditions and multiply by 10^4 , so that each $S_n(0)$ is now a random number uniformly distributed between zero and one, then we find the result in Fig. 8. With these large initial fluctuations in salinity none of the realizations synchronize and in two of the cases in Fig. 8 persis-

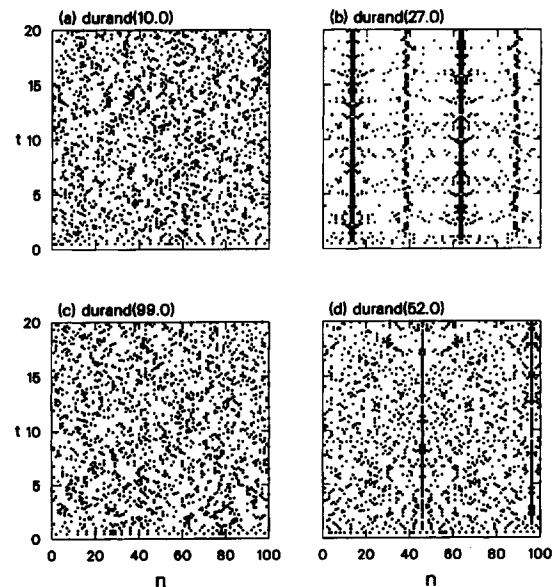


Fig. 8. Same as Fig. 7 except that $\alpha = 0.3$ and the initial condition is a random number uniformly distributed between 0 and 1. Centers of preferred adjustment are obtained also with this larger diffusivity.

tent centers of adjustment nucleate from the random initial conditions.

The simulations summarized in these sections display a bewildering variety of patterns which emerge from both random and structured initial conditions. Perhaps the most surprising result is the existence of centers of adjustment and the persistence of grid-scale structure. In Section 4 we will turn to some simple analytic considerations that help rationalize these observations.

4. Analytic models with small N

In this section we retreat to some analytic models in which the number of grid points is small. Our goal is to find some analytic solutions which demonstrate the existence of centers of adjustment and the associated suppression of adjustment at neighboring grid points.

4.1. Triplet solutions

In Section 3 we summarized the “grid mode” solution which had essentially two independent variables: $a(t)$ and $b(t)$. In this section we construct an analogous solution with three independent variables. Suppose that

$$\begin{aligned} S_{3n} &= a(t), \\ S_{3n+1} &= b(t), \\ S_{3n+2} &= c(t). \end{aligned} \tag{4.1}$$

and at $t = 0$ there has just been an adjustment so that $a(0) = 0$ while $b(0) = B$ and $c(0) = C$. We look for a solution in which the next adjustment is at $t = \frac{1}{3}$ and $a(\frac{1}{3}) = B$, $b(\frac{1}{3}) = C$ and $c(\frac{1}{3}) = 1 \rightarrow 0$. The dynamics in subsequent interval, $\frac{1}{3} < t < 2/3$, repeats what happened in the first interval, but with the replacement $a \rightarrow b$, $b \rightarrow c$ and $c \rightarrow a$. Thus at the end of three such intervals the system has returned to initial state.

The solution described above is a wave with wavelength $n = 3$ and period 1. The wave travels to the right because the first three grid points adjust in the or-

der 1, 2, 3 and so on. By symmetry there is also a left going wave in which the order of adjustment is 3, 2, 1 and so on. We refer to these solutions that are periodic in both space and time as “structured solutions”.

Because of the symmetry we have assumed the set of differential equations in (2.2a) reduces to

$$\begin{aligned} \dot{a} &= 1 + \mu(b + c - 2a), \\ \dot{b} &= 1 + \mu(a + c - 2b), \\ \dot{c} &= 1 + \mu(a + b - 2c). \end{aligned} \tag{4.2}$$

It is easy to explicitly solve this set in the interval $0 < t < \frac{1}{3}$ with the initial condition $a(0) = 0$, $b(0) = B$ and $c(0) = C$. Then at $t = \frac{1}{3}$ one can determine the constants B and C by requiring that the pattern has shifted one grid point to the right. The result is that

$$\begin{aligned} B &= \frac{1}{1 + \exp(-\mu) + \exp(-2\mu)}, \\ C &= \frac{1 + \exp(-\mu)}{1 + \exp(-\mu) + \exp(-2\mu)}. \end{aligned} \tag{4.3}$$

Notice that both B and C are less than one. One can also verify that $b(t)$ and $c(t)$ remain less than one throughout the interval $0 < t < \frac{1}{3}$. Thus we have a good solution of (2.2a), (2.2b).

When μ is large we see that $1 - C \approx \exp(-2\mu)$, which is the same exponentially small quantity that appeared in our earlier discussion of the grid mode e.g., see (3.4) and the surrounding discussion. Thus we expect that this traveling triplet solution puts the same demands on accuracy as the grid mode solution. (Incidentally, the grid mode is equivalent to a traveling doublet but in this case there is no distinction between a left and right going wave.)

Figure 9 shows the results of a numerical integration of the $N = 3$ version of (2.2). We have taken $\alpha = \frac{1}{2}$ so that $\mu \equiv \alpha N^2 = \frac{9}{2}$ and a time step $\tau = 10^{-5}$. In Fig. 9(a) we show the results of starting the system with an initial condition given by the analytic solution. The result is the 1–2–3 wave described above. In Fig. 9(b) this initial condition is perturbed slightly but the 1–2–3 wave eventually emerges. Thus the 1–2–3 solution has a finite basin of attraction. In Fig. 9(c) the strength of the initial perturbation is increased and a 3–2–1 wave emerges i.e., the direction of propagation

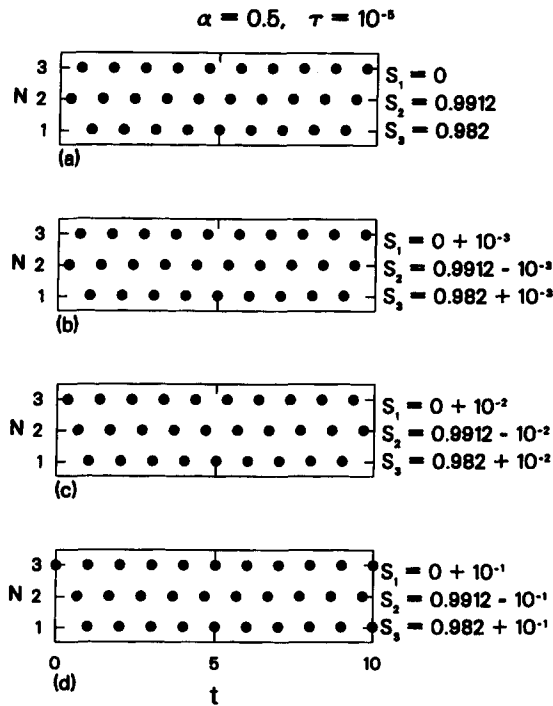


Fig. 9. The time-space coordinates of the CA events for a numerical integration of (2.3) and (2.4) with $\alpha = 0.5$, $N = 3$ and $\tau = 10^{-5}$ for different initial conditions. For some initial conditions the “traveling triplet” is obtained (upper three panels) and for other initial conditions a partially synchronized solution emerges.

of the wave of adjustment is now reversed. An even stronger perturbation, shown in Fig. 9(d), results in a partially synchronized solution in which grid points 1 and 3 are locked together and adjust in alternation with 2.

The result in Fig. 9(d) motivated us to look for such a partially synchronized, and periodic in time, solution. One sets $S_1(t) = S_2(t) = a(t)$ and $S_3(t) = c(t)$. (Of course, there are two other partially synchronized solutions that be constructed using the relabeling symmetry.)

Suppose that a “double adjustment” has just occurred at $t = 0$ so that $a(0) = 0$ and $c(0) = C$. Then a single adjustment occurs at $t = t_1$, so that $a(t_1) = A$ and $c(t_1) = 1 \rightarrow 0$. It turns out that the next double adjustment occurs at $t = 1$ so that the requirement of periodicity implies $a(1) = 1 \rightarrow 0$ and $c(1) = C$. One can solve the reduced version of (2.2a), analogous to

(4.2), in the two intervals $0 < t < t_1$ and $t_1 < t < 1$ and apply the various conditions above to obtain three equations for the three unknowns A , C and t_1 . The algebra is more complicated than the earlier calculations because this partially synchronized solution has fewer symmetries than either the grid mode or the traveling triplet. The transcendental equation that determines t_1 is

$$t_1 = \frac{2}{3} + \frac{1}{3} [1 - e^{-3\mu}]^{-1} \times [e^{-3\mu} - 2e^{-3\mu t_1} + e^{-3\mu(1-t_1)}], \quad (4.4a)$$

$$\approx \frac{2}{3} + \frac{1}{3} e^{-\mu}, \quad (4.4b)$$

where the approximation in (4.4b) requires that $\exp(-2\mu) \ll 1$. This same approximation also shows that

$$A \approx 1 - e^{-2\mu}, \quad (4.5a)$$

$$C \approx 1 - e^{-\mu}. \quad (4.5b)$$

Once again, we see that accuracy demands resolving the exponentially small quantity $\exp(-2\mu)$.

To summarize, with $N = 3$, we have six different periodic in time solutions. There is the synchronized solution, two solutions corresponding to left and right going waves, and three different partially synchronized solutions. Fig. 9 offers numerical evidence that some of these solutions have a finite basin of attraction. With these results we start to glimpse some of the complexity that emerged in Section 3 when we numerically solved the system with $N = 100$.

One issue that the $N = 3$ solutions do not address is the possibility of suppression of adjustment at some grid points and the concomitant formation of centers of adjustment at other grid points. To find such solutions we turn to $N = 4$.

4.2. Quartet solutions

With $N = 4$ one can obtain the traveling wave solutions which are analogous to the 1–2–3 wave described above. We defer discussion of this case till after we have examined a more interesting solution which exhibits suppression of adjustment.

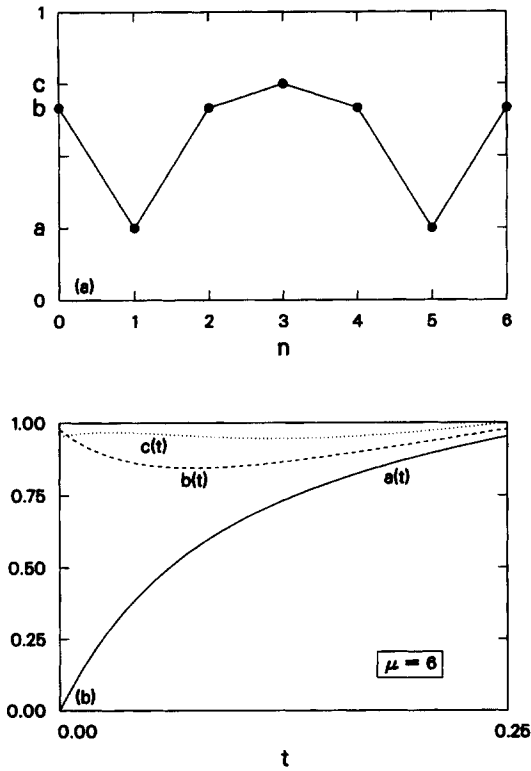


Fig. 10. (a) The spatial configuration for the quartet solution (4.6). Shown above is S_n for the seven grid point $n = 0$ to $n = 6$. Numbers 1–4 form a quartet according to the notation in (4.6). This configuration is then reproduced periodically along the n -axis. The points at $n = 2$ and $n = 4$ [i.e., $S_2(t) = S_4(t) = b(t)$] never undergo adjustment, while those corresponding $S_1(t)$ and $S_3(t)$ adjust in alternation at times separated by $\frac{1}{4}$. (b) The time evolution for $0 < t < \frac{1}{4}$ of the four salinity values $S_1 = a(t)$, $S_2 = S_4 = b(t)$ and $S_3 = c(t)$: at $t = \frac{1}{4}$, $c(t)$ reaches the CA threshold. For $\frac{1}{4} < t < \frac{1}{2}$, the roles of a and c are exchanged, while b is the same.

Consider the “symmetric quartet” configuration in Fig. 10(a). That is

$$\begin{aligned} S_1(t) &= a(t), \\ S_2(t) &= S_4(t) = b(t), \\ S_3(t) &= c(t). \end{aligned} \tag{4.6}$$

We now construct a periodic in time solution in which $a(t)$ and $c(t)$ alternately adjust while $b(t)$ never adjusts. Thus there are two adjustment centers and there is suppression of adjustment at the other two grid points. In order to motivate the construction we begin

by showing a plot of the solution in Fig. 10(b). At $t = 0$, $S_1(0) = a(0)$ has just adjusted so that $a(0) = 0$. At $t = \frac{1}{4}$, $S_3(\frac{1}{4}) = c(\frac{1}{4})$ adjusts so that $c(\frac{1}{4}) = 1 \rightarrow 0$. Also at $t = \frac{1}{4}$, $b(\frac{1}{4}) = S_2(\frac{1}{4}) = S_3(\frac{1}{4})$ have returned to their position at $t = 0$ so $b(\frac{1}{4}) = b(0)$. Finally at $t = \frac{1}{4}$ $a(\frac{1}{4}) = c(0)$. In the next interval, $\frac{1}{4} < t < \frac{1}{2}$, the motion repeats itself but with $a(t)$ and $c(t)$ exchanged. Thus the period is $\frac{1}{2}$, i.e., Fig. 10(b) shows half of one oscillation.

To determine the constants $B \equiv b(0)$ and $C \equiv c(0)$ one solves the reduced version of (2.2a) in the interval $0 < t < \frac{1}{4}$ and applies the various initial and final conditions. In this way one obtains

$$\begin{aligned} B &= \frac{1}{2} \left[\frac{1}{1 - e^{-\mu}} + \frac{1}{1 + e^{-\mu/2}} \right], \\ C &= \frac{1}{1 + e^{-\mu/2}}. \end{aligned} \tag{4.7}$$

However, we are not finished because we must still verify that all the variables remain below the threshold $S = 1$ during the interval $0 < t < \frac{1}{4}$. It turns out that this condition is equivalent to $1 > B(\mu)$. The function $B(\mu)$ is plotted in Fig. 11 and the condition that $1 > B(\mu)$ is equivalent to

$$2 \ln 2 < \mu. \tag{4.8}$$

This completes the construction of the symmetric quartet solution.

Recalling that $\mu \equiv \alpha N^2$ we see from (4.8) that the symmetric quartet is a possible solution provided that the coupling between adjacent grid points is

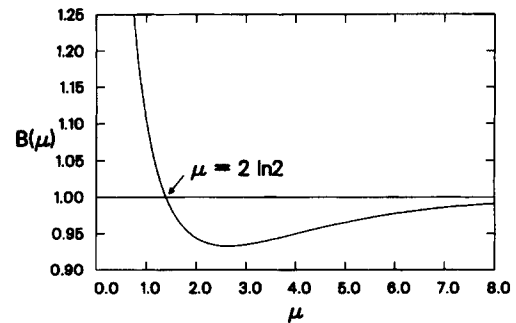


Fig. 11. A plot of $S_2(0) = S_4(0)$ as a function of the coupling parameter $\mu \equiv \alpha N^2$. Only values below unity are acceptable. Thus μ must exceed $2 \ln 2$.

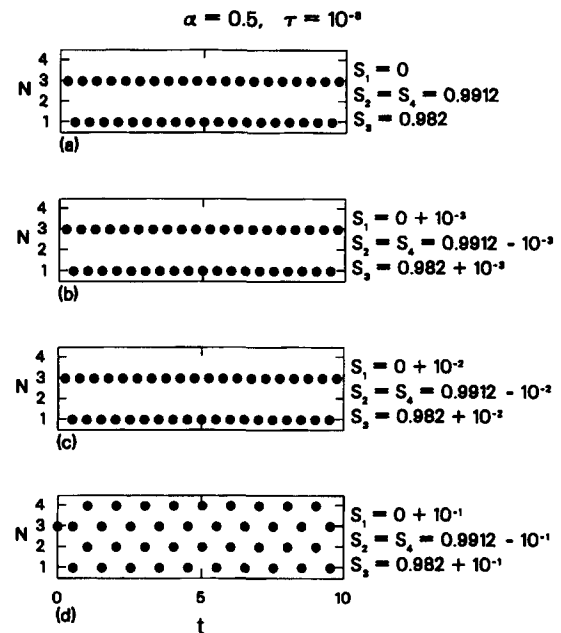
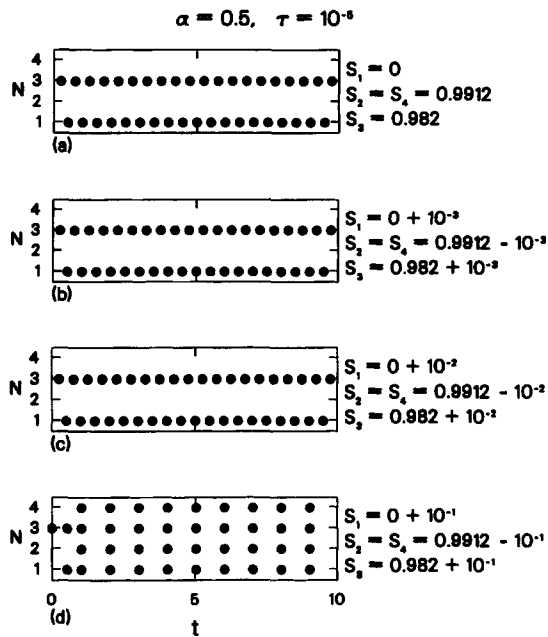


Fig. 12. The time–space coordinates of the CA events for a numerical integration of (2.3) and (2.4) with $\alpha = 0.5$, $N = 4$ and $\tau = 10^{-5}$ for initial conditions that are perturbations of (4.7), i.e., those leading to the exact “symmetric quartet” solution (4.6). For small perturbations the “symmetric quartet” is obtained (upper three panels) and for large perturbations (lowest panel) the synchronized solution is obtained.

Fig. 13. Same as Fig. 12 except that $\tau = 10^{-8}$, i.e., small enough to resolve the grid mode discussed in Section 3.1. The “symmetric quartet” solution, with suppressed CA at two points, is robust to small perturbations (upper three panels). Large perturbations lead to the emergence of the grid mode (lowest panel).

sufficiently strong. If μ is large then the results in (4.7) simplify to

$$B \approx 1 - \frac{1}{2}e^{-\mu/2}, \quad C \approx 1 - e^{-\mu/2}. \quad (4.9)$$

To accurately represent the solution that we have found above a computer must be able to distinguish between B and 1. This resolution requirement is much weaker than those associated with our earlier solutions because $\exp(-\mu/2) \gg \exp(-2\mu)$ when μ is large.

Figure 12 shows the results of integrating the system (2.2) with $N = 4$ and $\alpha = \frac{1}{2}$, so that $\mu = 8$. The time step is $\tau = 10^{-5}$ which satisfies the double inequality $e^{-2\mu} \ll \tau \ll e^{-\mu/2}$.

$$(4.10)$$

The inequality above ensures that the grid mode is suppressed, while the symmetric quartet is resolved. In Fig. 12(a) the initial condition is given by the analytic result in (4.7). The three successive parts of Fig. 12 show the results of perturbing this symmetric quartet

initial condition. In Figs. 12(b) and (c) the symmetric quartet solution attracts the perturbed initial condition. But for the large initial perturbation in Fig. 12(d) the synchronized solution is the final state of the system.

If the calculations in figure are repeated with a much smaller time step, $\tau = 10^{-8}$, so that now

$$\tau \ll e^{-2\mu} \ll e^{-\mu/2}, \quad (4.11)$$

then the grid mode is no longer suppressed by the roundoff error. The result is shown in Fig. 13. In Fig. 13(a) the system is started precisely on the symmetric quartet solution it remains there. Figs. 13(b), (c) and (d) show that the symmetric quartet solution is stable to small perturbations even when the grid mode is allowed. The grid mode, however, emerges for large perturbations, instead of the synchronized solution (cf. Fig. 12(d) with Fig. 13(d)). Thus with the very small time step, $\tau = 10^{-8}$, we are accurately solving the semi-discrete system in (2.2) and the grid mode emerges as well as the symmetric quartet solution.

To complete our discussion of structured solutions for $N = 4$ we consider the “traveling quartet”, which is the analog of the traveling triplet discussed in Section 4.1. We remove the symmetry (4.6b), so that all four points have distinguished values at $t = 0$. Thus $S_1(0) = 0$, $S_2(0) = B$, $S_3(0) = C$ and $S_4(0) = D$. At $t = \frac{1}{4}$ we require that the pattern has shifted by one grid point to the right. That is: $S_1(\frac{1}{4}) = D$, $S_2(\frac{1}{4}) = 1 \rightarrow 0$, $S_3(\frac{1}{4}) = B$ and $S_4(\frac{1}{4}) = C$. A straightforward calculation then shows that

$$\begin{aligned}
 B &= \frac{2 + \exp(-\mu/2)}{2 + 2 \exp(-\mu)}, \\
 C &= \frac{1}{1 + \exp(-\mu)}, \\
 D &= \frac{2 - \exp(-\mu/2)}{2 + 2 \exp(-\mu)}.
 \end{aligned}
 \tag{4.12}$$

The requirement that all the points are below the threshold during the interval $0 < t < \frac{1}{4}$ implies that

$$\mu < 2 \ln 2.
 \tag{4.13}$$

Remarkably, this condition is complementary to the condition in (4.8) which is required for the existence of the symmetric quartet.

4.3. Implications for larger values of N

The methods we have used to construct periodic solutions with $N = 2, 3$ and 4 can be applied to larger values of N . For instance it is possible to find a traveling wave solution with spatial period N and temporal period 1. The wave translates one grid point every $\Delta t = 1/N$. This is the generalization of the $N = 4$ traveling wave in (4.12). The existence of this solution requires that the coupling coefficient μ satisfies an inequality analogous to (4.13), with the maximum value of μ approaching unity as N increases.

When N is even there is also a “symmetric N -tet” solution in which two antipodal grid points adjust in alternation and the remaining $N - 2$ grid points never adjust. The period of this N -tet oscillation is $2/N$. The existence of the symmetric N -tet solution requires that the coupling coefficient, μ , satisfy an inequality analogous to (4.8). The minimum value of μ increases with

increasing N . The patterns of adjustment in Figs. 4(b) and (c) seem to be noisy versions of this solution.

To summarize, when N is large the system in (2.2) has many exact solutions that are periodic both in space and time. Each of these periodic solutions has a “basin of attraction” in the space of initial conditions. With large values of N this can result in complicated behavior because of the many alternative ways of constructing periodic solutions, e.g., if $N = 100$ we could in principle look for traveling wave solutions with any spatial periods that divides evenly into 100 or, if μ is large enough, a symmetric solution in which just two grid points adjust and the remaining 98 never adjust.

However, obtaining these structured solutions numerically requires resolving some exponentially small quantity, so that the time step must satisfy an inequality of the form

$$\tau < \exp(-q\mu).
 \tag{4.14}$$

The constant q depends on the details of the solution: for the grid mode $q = 2$, for the symmetric quartet $q = \frac{1}{2}$, and for the symmetric N -tet $q = 2/N$. Generally, q becomes smaller as the temporal period becomes shorter. This is so because each adjustment event forces the grid mode. This mode then decays in between adjustment events with an e-folding time of 4μ . Thus if the time between adjustment events is Δt then the grid mode has decayed by a factor of $\exp(-4\mu\Delta t)$ by the time the next event occurs. This implies that the value of S at some nonadjusting grid point differs from one by $\exp(-4\mu\Delta t)$. This exponentially small quantity must be resolved in order to accurately compute the structured solution.

5. Conclusion

Convective adjustment algorithms that are based on applying a rule have an unphysical sensitivity to numerical errors and slight changes in time step, spatial resolution and initial condition. Indeed, as we have repeatedly emphasized, the dependence on the spatial resolution is exponentially strong. It may be that alternative strategies, such as implicit vertical diffusion (e.g., [2]) avoid these problems. Implicit vertical

diffusion schemes increase the strength of the vertical mixing coefficient to some large, but finite, value when the layer is statically unstable. Thus density inversions are removed rapidly, but not instantaneously.

Based on our results we can identify a nondimensional parameter which characterizes implicit vertical diffusion schemes. This is the ratio of the horizontal diffusion time between grid points ($1/4\mu$ in our case) to the time scale for vertical mixing (zero in our case). We expect that when this parameter is large (i.e., when horizontal mixing is slower than the vertical mixing) then implicit vertical diffusion schemes will probably display the same sensitivity as the instantaneous adjustment model considered in this paper.

Recent models of oceanic convection [13–15] emphasize that the rim current enclosing a convective chimney is baroclinically unstable. The ensuing fragmentation of the chimney produces lateral mixing. Thus the vertical and lateral mixing processes triggered by oceanic convection are coupled. It is precisely this aspect of the physical problem which is ignored by the convective adjustment rules we have criticized in this paper. So the challenge facing us now is to formulate a physically motivated parameterization of convection that accounts for the coupling between vertical and lateral mixing.

Acknowledgements

This research was supported by the CHAMMP program (DOE DEFG 03 93ER61690). We thank Lisa Lehman for her invaluable assistance with the computations.

References

- [1] F. Bryan, High latitude salinity effects and interhemispheric thermohaline circulations, *Nature* 323 (1986) 310.
- [2] J. Marotzke, Influence of convective adjustment on the stability of the thermohaline circulation, *J. Phys. Oceanogr.* 21 (1991) 903.
- [3] F.L. Yin and E.S. Sarachick, An efficient convective adjustment scheme for ocean general circulation models, *J. Phys. Oceanogr.* 24 (1994) 1425.
- [4] J.D. Keeler and J.D. Farmer, Robust space-time intermittency and $1/f$ noise, *Physica D* 23 (1986) 413.
- [5] J.P. Crutchfield and K. Kaneko, Phenomenology of spatio-temporal chaos, in: *Direction in Chaos*, ed. Hao Bai-Lin (World Scientific, Singapore, 1987) p.272.
- [6] P. Cessi, Grid-scale instability of convective-adjustment schemes, *J. Mar. Research.*, accepted.
- [7] H. Stommel, Thermohaline convection with two stable regimes of flow, *Tellus* 13 (1961) 224.
- [8] M. Winton, Deep decoupling oscillations of the oceanic thermohaline circulation, in: *Ice in the Climate System*, NATO ASI series, Vol. 112, ed. W.R. Peltier, (Springer, Berlin, 1993) p.417.
- [9] D.W. Pierce, T.P. Barnett and U. Mikolajewicz, Competing role of heat and freshwater flux in forcing thermohaline oscillations, *J. Phys. Oceanogr.* 25 (1995) 2046.
- [10] K. Bryan, A numerical method for the study of the circulation of the world ocean, *J. Comput. Phys.* 4 (1969) 347.
- [11] P. Welander, A simple heat-salt oscillator, *Dyn. Atmos. Oceans* 6 (1982) 233.
- [12] P. Cessi, Convective adjustment and thermohaline, excitability, *J. Phys. Oceanogr.*, in press.
- [13] U. Send and J. Marshall, Integral effects of deep convection, *J. Phys. Oceanogr.* 25 (1995) 855.
- [14] H. Jones and J. Marshall, Convection with rotation in a neutral ocean: A study of open ocean deep convection, *J. Phys. Oceanogr.* 23 (1993) 1009.
- [15] S. Legg and J. Marshall, A heton model of the open-ocean spreading phase of deep convection, *J. Phys. Oceanogr.* 23 (1993) 1040.